Supporting Material, Defining the limits of single-molecule FRET resolution in TIRF microscopy

Seamus J. Holden[1,2], Stephan Uphoff[1], Johannes Hohlbein[1], David Yadin[1], Ludovic Le Reste[1], Oliver J. Britton[1], and Achillefs N. Kapanidis[1,2]

[1]Biological Physics Research Group, Clarendon Laboratory, Department of Physics, University of Oxford, UK

[2]Corresponding authors. Address: Clarendon Laboratory, University of Oxford, Parks Road, Oxford, OX1 3PU, UK. Email: s.holden1@physics.ox.ac.uk, a.kapanidis1@physics.ox.ac.uk

Contents

Theory

Thompson et al. (1) derived predictions for the photon-counting error of a conventional CCD camera without an electron multiplying gain register. We use a slightly modified version of this derivation, and include electron multiplication effects, noting important experimental considerations which must be taken into account. We also explicitly derive predictions (implied in Thompson's work) for photon-counting error, and predictions which include pixelation effects and do not interpolate in the regime where the effects of shot noise and background noise are of similar magnitude.

Having obtained photon-counting error predictions for a single channel, we extend this result by error propagation (2) to obtain predictions for the expected heterogeneity on a FRET measurement.

Photon counting error for an emCCD

Fluorescence emission photons are collected from a surface-immobilized biomolecule and focused onto an electron multiplying CCD (emCCD) camera. The photons collected on a single pixel within the integration time for a single image frame generate electrons amplified in the electron multiplying gain register of the camera to reduce the effective read noise of the device (3). The amplified electron count is converted to digital units (DU) by the analogue to digital converter. It is these DU which form the pixel counts in the final image of fluorescence emission. For an individual channel M, DUs and photon count are related by:

$$M_{DUij} = UM_{ij}, \quad U = G/C. \tag{S1}$$

M_{DUij} and M_{ij} are the number of DU and photons collected on a single pixel with index ij, respectively. U is the effective gain (DU/photon), determined by G, the electron multiplying gain (electrons/photon), and C, the CCD sensitivity (electrons/DU). The value of C may be obtained from the camera manufacturer. G is set by the operator and is typically 100-1000 (4). However, G frequently differs significantly from the manually set value, due primarily to aging of the EM gain register (5). For photon-counting applications U should be measured directly on a regular (at least annual) basis using standard methods (6, 7). The photon count M_{ij} may then be calculated from the pixel count M_{DUij} by Eq. S1.

Modifying Thompson's result (1) to include effects of electron multiplication, the expected variance on measured photon count for a single pixel is

$$\sigma_{ij}^2 = f_G^2 M_{ij} + b^2. \tag{S2}$$

f_G is the excess noise factor introduced by the electron multiplication (4). For typical values of G (100-1000), $f_G = \sqrt{2}$ to good approximation (4). The term $f_G^2 M_{ij}$ represents the total contribution of photon-counting shot noise taking into account excess noise from electron multiplication. b is the observed standard deviation of background noise per pixel (excluding photon-counting shot noise), including background in the measurement and any on-camera noise due to read noise and dark noise, which for an emCCD we expect to be very small. We neglect digitization noise (3) since

its effect for typical experimental parameters is a correction of $<$0.1% (unpublished data). We neglect dead time and smearing due to frame transfer (3), since for currently available fluorophores, maximal photon emission rates are such that these effects are not significant.

To obtain a prediction of photon-counting error for a surface-immobilized molecule located at (x_0, y_0), with total expected photon count M_0 and independent Gaussian distributed errors, we begin with the criterion of least-squares fitting, that χ^2,

$$\chi^2(x, y, M) = \sum_{i,j} \frac{\{m_{ij} - M_{ij}(x, y, M)\}^2}{s_{ij}^2}, \tag{S3}$$

is minimized, where m_{ij} is the observed photon count, M_{ij} is the photon count expected from a model PSF located at (x, y) with total photon count M, and s_{ij}^2 is the observed photon count variance (distinct from the expected variance σ_{ij} defined by Eq. S2).

We note the criterion of least-squares minimization for Gaussian distributed errors derives from minimization of the exponent term of the multivariate normal distribution (8). However, since the variance term appears not only in the exponent of this distribution, but also in its normalization term, it follows that the variance must be held fixed during least-squares minimization for independent Gaussian distributed errors. Therefore, it is most appropriate to use the observed (rather than the expected) variance in minimization of Eq. S3, assuming the sample size is sufficiently large that the observed variance is a good estimate of the "true" population variance (this criterion being imposed in our derivation by calculating the expectation value of s_{ij}^2 in Eq. S5).

Using the condition for the minimum, $\partial \chi^2 / \partial M = 0$, we expand $M_{ij}(x, y, M)$ about $M_{ij}(x_0, y_0, M_0)$. Considering only first order terms in $\Delta M = M - M_0$, and noting that $\partial s_{ij}^2 / \partial M = 0$, we obtain:

$$\Delta M \sim -\frac{\sum\limits_{i,j} \Delta m_{ij} \frac{\partial M_{ij}}{\partial M} / s_{ij}^2}{\sum\limits_{i,j} \left(\frac{\partial M_{ij}}{\partial M} / s_{ij}\right)^2}, \tag{S4}$$

where $\partial M_{ij} / \partial M$ is evaluated at $M_{ij}(x_0, y_0, M_0)$, and $\Delta m_{ij} = M_{ij}(x_0, y_0, M_0) - m_{ij}$. Squaring Eq. S4, calculating the expectation value, and using $\sigma^2(M) = \langle (\Delta M)^2 \rangle$ (because $\langle (\Delta M) \rangle^2 = 0$), yields

$$\sigma^2(M) = \left\{ \sum_{i,j} \left(\frac{\partial M_{ij}}{\partial M}\right)^2 / \langle s_{ij}^2 \rangle \right\}^{-1}. \tag{S5}$$

Using the fact that the expectation value of the observed variance $\langle s_{ij}^2 \rangle$ equals the expected variance σ_{ij}^2 defined by Eq. S2, we obtain,

$$\sigma^2(M) = \left\{ \sum_{i,j} \left(\frac{\partial M_{ij}}{\partial M} / \sigma_{ij}\right)^2 \right\}^{-1}. \tag{S6}$$

We assume a circular 2D Gaussian PSF,

$$M_{i,j} = \frac{M}{2\pi s^2} \exp\left(\frac{(i - x_0)^2}{2s^2} + \frac{(j - y_0)^2}{2s^2}\right) + B_M. \tag{S7}$$

(i, j) are the pixel coordinates. (x_0, y_0) is the position of the molecule. M is the total expected photon count, M_{ij} is the expected photon count at pixel (i, j). s is the width of the PSF. B_M is the expected background level.

If we neglect pixelation effects, we may replace Eq. S6 with an integral:

$$\sigma^2(M) \sim \left\{ \int \int \left(\frac{\partial M_{ij}}{\partial M} / \sigma_{ij} \right)^2 di \, dj \right\}^{-1}. \tag{S8}$$

If we substitute Eq. S7 into Eq. S8 and assume (following Thompson) that in the intermediate regime where $f_G^2 M_{ij} \sim b^2$, $\sigma(M)$ is well approximated by the sum of the limiting cases when the first and then the second terms in Eq. S2 dominate, we obtain:

$$\sigma^2(M) = f_G^2 M + \frac{4\pi s^2}{a^2} b^2. \tag{S9}$$

To include pixelation effects and avoid interpolation where $f_G^2 M_{ij} \sim b^2$, we must substitute Eq. S7 into Eq. S6, and average over all (x_0, y_0):

$$\langle (\sigma^2(M) \rangle_{x_0, y_0} = \frac{\int_{-\infty}^{\infty} \int_{-\infty}^{\infty} \sigma^2(M) dx_0 dy_0}{\int_{-\infty}^{\infty} \int_{-\infty}^{\infty} dx_0 dy_0}. \tag{S10}$$

By symmetry, each pixel is equivalent with respect to (x_0, y_0), allowing us to reduce our range of integration to one pixel in each direction. For square pixels of width a, this yields:

$$\langle (\sigma^2(M) \rangle_{x_0, y_0} = a^{-2} \int_0^a \int_0^a \left\{ \sum_{i,j=-\infty}^{i,j=\infty} \left(\frac{\partial M_{i,j}}{\partial M} / \sigma_{i,j} \right)^2 \right\}^{-1} dx_0 dy_0. \tag{S11}$$

Expected FRET measurement error

To obtain a prediction for FRET error, we perform error propagation (2, 9), assuming D and A are independently distributed, for apparent FRET, E:

$$E = A/N, \quad N = D + A. \tag{S12}$$

where D, A and N are the donor, acceptor, and total photon counts for an individual molecule, respectively. Then

$$\sigma(E) = \sqrt{\left(\frac{\partial E}{\partial D} \right)^2 \sigma^2(D) + \left(\frac{\partial E}{\partial A} \right)^2 \sigma^2(A)}, \tag{S13}$$

which simplifies to

$$\sigma(E) = \frac{1}{N} \sqrt{E_0^2 \sigma^2(D) + (1 - E_0)^2 \sigma^2(A)}, \tag{S14}$$

where E_0 is the mean FRET value.

For the full prediction of $\sigma(E)$, we numerically integrate Eq. S11 for each channel, and substitute the results into Eq. S14.

If we neglect pixelation and interpolate between the high shot noise and high background limits, then using Eq. S9 we obtain:

$$\sigma(E) = \sqrt{\frac{f_G^2 E_0(1 - E_0)}{N} + \frac{4\pi}{a^2 N^4}\left(D^2 s_D^2 b_D^2 + A^2 s_A^2 b_A^2\right)}. \tag{S15}$$

E_0 is the mean FRET value. s_D, s_A are the PSF widths in donor and acceptor channels. b_D , b_A are the standard deviations (photons per pixel) of observed background noise in each channel. a is the pixel size. f_G is the excess noise factor.

Instrumentation

We used a custom-built objective-type TIRF apparatus (Figure S1) to collect smFRET data for fluorescently labeled dsDNA immobilized on a microscope coverslip. A green laser (532 nm, continuous-wave solid state laser, Samba model, Cobolt, Sweden; modulated using an acousto-optical modulator from AA Optics, France) and a red laser (635 nm, directly modulated diode laser, Cube model, Coherent, USA) operated in ALEX mode (10–12) were combined via a dichroic mirror and coupled into an optical fiber. The output of the fiber was focused onto the back-focal-plane of the objective lens (100x oil immersion objective, NA 1.4, Olympus, Japan), displaced from the center of the optical axis such that the excitation light was incident upon the coverslip at an angle greater than the critical angle for total internal reflection, generating an exponentially decaying evanescent wave with a decay constant of $\sim$100 nm (13), in order to selectively excite only a small volume adjacent to the coverslip (13, 14). All experiments were carried out at laser powers of 2 mW (532 nm) and 1 mW (635 nm). An integration time of either 20 ms with 50 Hz alternation and frame rate, or of 100 ms with 10 Hz alternation and frame rate, was used, the choice for each experiment being specified in the main text. A motorized xy-scanning stage (MS-2000, ASI Imaging, USA) was used to control the coverslip position relative to the objective.

Emission fluorescence was collected by the objective lens and separated from the excitation light using a dichroic mirror (545 nm/ 650 nm, Semrock, USA) and additional filters (545 nm LP, Chroma, USA; and 633/ 25 nm notch filter, Semrock, USA). The emission fluorescence was then focused through an aperture to make the field of view of view rectangular, and spectrally separated into green and red emission channels via a dichroic mirror (630 nm DRLP, Omega, USA). The two emission channels were focused side by side onto an emCCD camera (Andor iXon 897, UK), with pixel size a measured as 94 nm.

DNA sequences

The sequences and positions of labels for all dsDNA FRET standards used in this work (shown in Figure 1) are listed below. X indicates a 5-C6-Amino-dT, labeled with ATTO647N. Y indicates a

5'-Amino-C6, labeled with Cy3B, except for FRET standard number 5, where Y indicates a 5-C6-Amino-dT, labeled with Cy3B. Amino-modified biotinylated top strand, and amino-modified bottom strand single-stranded DNA was purchased from IBA (Gottingen, Germany). Top strands were labeled with Cy3B, bottom strands with ATTO647N, and purified using denaturing PAGE. Strands were annealed by mixing equimolar amounts of top and bottom strand in annealing buffer (Tris-HCl *pH* 8.0, 500 mM NaCl, 1 mM EDTA), and heating to 95°C, followed by slow cooling to 4°C.

1. T1B16

```
Top:     Y-5'-TAAATcTAgTAAcATAAggTAAcATAAcgTAAgcTcATTcgcg-3'-Biotin
Bottom:   3'-ATTTAgATcATTgTAXTccATTgTATTgcATTcgAgTAAgcgc-5'
```

2. T1B17

```
Top:     Y-5'-TAAATcTAAgTAAcATAAggTAAcATAAcgTAAgcTcATTcgcg-3'-Biotin
Bottom:   3'-ATTTAgATTcATTgTAXTccATTgTATTgcATTcgAgTAAgcgc-5'
```

3. T1B18

```
Top:     Y-5'-TAAATcTAAAgTAAcATAAggTAAcATAAcgTAAgcTcATTcgcg-3'-Biotin
Bottom:   3'-ATTTAgATTTcATTgTAXTccATTgTATTgcATTcgAgTAAgcgc-5'
```

4. T1B18GC

```
Top:     Y-5'-ccgATcTAAAgTAAcATAAggTAAcATAAcgTAAgcTcATTcgcg-3'-Biotin
Bottom:   3'-ggcTAgATTTcATTgTAXTccATTgTATTgcATTcgAgTAAgcgc-5'
```

5. T1B18INT

```
Top:     5'- gcgTTgcAYAAATcTAAAgTAAcATAAggTAAcATAAcgTAAgcTcATTcgcg-3'-Biotin
Bottom: 3'- cgcAAcgTATTTAgATTTcATTgTAXTccATTgTATTgcATTcgAgTAAgcgc-5'
```

Sample preparation

Biotinylated dsDNAs at a concentration of ∼50 pM were surface-immobilized on a polyethylene-glycol coated coverslip (15). We used silicone gaskets (Grace Bio-Labs, USA), covered with an additional glass coverslip to seal the imaging chambers from oxygen. To minimize photo-physics, we used an imaging buffer containing an oxygen-scavenging system and a triplet-state quenching agent: phosphate buffered saline (PBS), *pH* 7.4, 2 mM TROLOX (6-hydroxy-2,5,7,8-tetramethylchroman-2-carboxylic acid), 1% w/v glucose, 2 mg/ml glucose oxidase, and 80 μg/ ml catalase.

Monte Carlo simulations

We carried out Monte Carlo simulations to model tFRET data, including the Poisson noise on detected photons, explicit simulation of electron multiplying gain, simulation of the analogue to digital converter, a general background noise term, and pixelation effects. In order to separate the

effects of different noise sources, we carried out simulations which neglected the effect of multiple overlapping molecules, by simulating an isolated single molecule randomly positioned within a single pixel at the center of a small area (24×24 pixels). In separate simulations, presented below, we analyzed the errors introduced by the presence of multiple overlapping molecules using simulations of multiple molecules of varying surface density, randomly positioned within an area of 256×256 pixels. In each case, the position of a molecule was randomly chosen with sub-nanometer accuracy, and we simulated the effects of pixelation using pixel size, a, of 94 nm and PSF widths matching experimental values (typically ∼130 nm in the donor channel and ∼150 nm in the acceptor channel).

We assume that photon counts in the donor and acceptor channels are independently Poisson distributed variables (16), with mean values

$$\langle D \rangle = N(1 - E_0), \quad \langle A \rangle = NE_0. \tag{S16}$$

Molecular PSFs are modeled as 2D circular Gaussians (Eq. S7) with a total photon count (ie. volume) determined by Eq. S16. The photon count arising from a single molecule for each pixel is then drawn from a Poisson distribution with mean equal to the value of the PSF at that pixel.

We model electron multiplying gain for a 526-stage gain register (matching that of the camera used for experiments). Although it is straightforward to explicitly model each stage of a multi-stage gain register (17), this is an exceedingly slow process. Instead we perform rejection sampling (18) of the approximate probability density function for electron counts resulting from a gain register (17):

$$P(n) \begin{cases} = \frac{(n-m+1)^{m-1}}{(m-1)!(G-1+1/m)^m} \exp\left(-\frac{n-m+1}{G-1+1/m}\right) & \text{if } n \geq m, \\ = 0 & \text{otherwise,} \end{cases} \tag{S17}$$

where n is the final electron count, m is the input photon count and G is the electron multiplying gain. This expression has been shown to be accurate for even low values of G (17), and use of this algorithm produces a speed increase of a factor of ∼1000. We simulate the analogue to digital converter by calculating the conversion from electrons to DUs and rounding the result. Finally, we include a general background noise term by adding Gaussian distributed noise with standard deviation $b_{DU} = Ub$ (b_{DU} is the noise measured in DU, U is the effective gain, b is the noise measured in photons), rounding the final result.

Simulations with one molecule per image were written in MATLAB. Simulations with multiple molecules per image were written in C++.

Image analysis

To optimize extracted signal-to-noise and ensure statistical robustness of data, it is important to automate the data extraction from tFRET movies. To this end, we built on previous work within the field of single molecule biophysics (1, 19–22) and in astronomy (23–27), which deals with the similar problem of accurate photon-counting for multiple overlapping diffraction limited PSFs using CCDs. We designed and implemented highly-automated and robust image analysis software (to

be shortly released to the community). Image analysis code was written in MATLAB, except for the PSF-fitting code which was written as a C++ library with a MATLAB interface.

Our source data consists of synchronized movies of fluorescence emission in the donor and acceptor emission channels from multiple randomly distributed surface-immobilized single molecules. Image analysis for tFRET consists of 5 essential steps: *image registration*, *detection & localization*, *association*, *photometry* and *filtering*.

Image registration

Image registration is the process of generating a spatial mapping between the donor and acceptor coordinate systems. We apply the simple method of calibration using the leakage of acceptor emission of immobilized fluorescent beads into the donor channel to identify matching positions in each channel (19, 28). These "control points" are manually selected using a simple GUI and a spatial mapping is generated between the coordinate systems by solving

$$\mathbf{x_A} = \mathbf{T}\mathbf{x_D}, \tag{S18}$$

where $\mathbf{T}$ is a projective transformation matrix, $\mathbf{x_D}$ are the donor control points and $\mathbf{x_A}$ are the acceptor control points. The resulting quality of alignment is checked visually using a color-coded overlay of the green and red channels. The semi-automatic nature of this task is acceptable since it is only necessary to perform it at most once for a daily set of experiments, however it should be straightforward to automate this task (29, 30).

Detection & localization

Detection and localization are the steps of automatically detecting molecules, and localizing their centroid. This step is performed separately in each channel. For detection, the classic approach is to apply a high pass spatial filter to remove noise, followed by convolution with a Gaussian mask of size similar to the candidate molecules, followed by identification of above-threshold pixels (22, 23, 26). We exploit the fact that molecules are immobilized and therefore only perform auto-detection and localization at the beginning of a movie, averaging typically 5-10 frames to maximize signal-to-noise.

To localize the centroid to high precision, we fit the detected molecules with an elliptical 2D Gaussian (Eq. 7) using ordinary-least-squares minimization, with the molecule's position (x_0, y_0) set as a free parameter. The fitting algorithm is identical to that employed for photometry, discussed shortly.

Point matching

Point matching is the process of matching detected molecules in the donor channel with molecules in the acceptor channel. If our data were entirely free from noise and optical aberrations, and our coordinate transform matrix was perfectly accurate it would be possible to assume that the position of a donor molecule in the acceptor channel is exactly given by Eq. S18. However,

primarily due to an imperfect transformation matrix, it is necessary to account for the remaining differences between the apparent positions of a molecule in each channel, or inaccurate photon counts would result. We achieve this by carrying out distance-based hierarchical clustering (31) for both the acceptor channel positions $\mathbf{x_A}$ and the transformed donor channel positions $\mathbf{Tx_D}$. Clusters containing zero or one molecules in each channel are retained, whereas clusters with ambiguous stoichiometry (for example a cluster containing two donor molecules and one acceptor) are discarded.

Photometry

Photometry is the term given in astronomy to the measurement of photon counts. Our algorithm of choice is *profile-fitting photometry* (25, 26, 32–35): fitting of a model PSF profile to an identified molecule. We fit Eq. 7 to a square subimage of width $2w_{im}$[1], centered on the position identified during the localization step. We use the Lourakis implementation (36) of constrained Levenberg-Marquardt optimization (37) to carry out *ordinary-least-squares (OLS) minimization* (37) of Eq. 8. For algorithmic speed, we set the coordinates (x_0, y_0) as constants (although it is straightforward to relax this assumption if experimental factors such as stage drift are significant). This algorithm implicitly assumes uniform noise across the whole image.

An alternative profile-fitting photometry algorithm is *weighted-least-squares (WLS) minimization* defined by Eq. S3 and used eg. by Thompson et al. (1). OLS implicitly assumes uniform noise the image, whereas WLS explicitly models the noise for each pixel. In principle, where uniform noise cannot be assumed (as in our case due to additional photon-counting shot noise arising directly from the immobilized molecule), WLS might optimize signal-to-noise where OLS fails to do so.

The simplest method available, and one commonly employed for tFRET measurements is *aperture photometry* (19–21, 24, 38). This is carried out by creating apertures, defined by radii r_1, r_2 and r_3 centered around a molecule. The total collected number of photons is estimated from pixels falling within the aperture defined by $r(ij) < r_1$, and the background is estimated from pixels within the annulus defined by $r_2 < r(ij) < r_3$ (we generally set $r_1 = r_2$). The background-subtracted photon count is thus

$$M_{ap} = \sum_{r(ij)<r_1} M_{ij} - \frac{n_{pix}}{n_B} \sum_{r_2<r(ij)<r_3} M_{ij}, \tag{S19}$$

where n_{pix} is the number of pixels within the inner circle, and n_B is the number of pixels in the annulus,

$$n_{pix} = \sum_{r(ij)<r_1} 1, \quad n_B = \sum_{r_2<r(ij)<r_3} 1. \tag{S20}$$

Variant methods include the use of square apertures (19–21) and time-averaging the background value over a number of adjacent frames to reduce noise (20). We note that the noise predictions differ from those obtained for profile fitting (27), and therefore derive a prediction for FRET error

---

[1]We define the subimage width as $2w_{im}$ for simplicity of comparison with methods which use a circular subimage of radius w_{im}

on an aperture photometry measurement. The photon-counting error for aperture photometry is given to good approximation (27) by

$$\sigma_{ap}^2(M) = f_G^2 M + \alpha b^2, \quad \alpha = n_{pix}\left(1 + \frac{n_{pix}}{n_B}\right). \tag{S21}$$

Applying error propagation, we derive a prediction for aperture photometry FRET measurement error,

$$\sigma_{ap}(E) = \sqrt{\frac{f_G^2 E_0(1 - E_0)}{N} + \frac{1}{N^4}\left(D^2\alpha_D b_D^2 + A^2\alpha_A b_A^2\right)}, \tag{S22}$$

where E_0 is the mean FRET value, D, A and N are the donor, acceptor and total photon counts. b_D and b_A are standard deviations of background noise in the donor and acceptor channels. α_D and α_A are defined in each channel by Eq. S21.

We examined the performance of the different methods (Figures S2-S3) for an effective window radius of 6 pixels ($\sim 4s$) and typical experimental parameters specified in the Materials & Methods. We set s_D=132 nm and s_A=150 nm. Considering first the photon-counting performance (Figure S2), we see that OLS shows the smallest systematic error, but shows a constant $\sim$25% excess noise compared to theoretical predictions. WLS asymptotically approaches optimal signal-to-noise, confirming that it is noise introduced by OLS fitting which causes the 25% (this finding is supported by previous reports (1, 39)). However, WLS shows significant systematic photon-counting errors, consistent with the literature (40, 41). In particular, the size of WLS systematic error varies as a function of total photon count, making it unsuitable for accurate measurements. Aperture photometry shows the greatest noise at low photon counts, however for high photon counts it approaches optimal signal-to-noise. Aperture photometry shows $\sim$4% systematic photon-counting errors, particularly in the acceptor channel, which has a larger PSF width[2]. Systematic errors for aperture photometry also cause an eventual increase in observed noise in the acceptor channel (Figure S2B).

Next, we analyzed FRET measurement performance of the different methods (Figure S3). OLS and WLS show the best performance at low photon counts, with WLS and aperture photometry showing the best performance at high photon counts. At extreme FRET values (E_0=0.1 or 0.9) the performance of aperture photometry suffers because of the low photon counts in one of the channels (Figure S3C). Because FRET is a ratiometric method, the systematic errors observed for WLS and aperture photometry photon counts largely cancel out for FRET measurements; systematic FRET measurement error for either method is effectively negligible.

Why then do we still recommend the use of OLS profile fitting as our algorithm of choice? We discount first the WLS method because in practice we found it to be rather unstable, requiring good initial estimates of background level and background noise, and knowledge of the effective gain, U.

Considering aperture photometry, the method offers acceptable and in some cases better signal-to-noise performance than OLS, and high computational speed. However, we find that OLS is generally a more robust method. OLS shows negligible systematic photon-counting errors, even for quite small effective window radii, w_{im}, whereas aperture photometry requires care in the

---

[2]We note that approaches exist to correct for these systematic errors (38, 42)

choice of aperture size to avoid systematic errors. We also find that OLS is less error prone in the presence of nearby or overlapping molecules. Where x-y stage drift or focal drift is an issue, by relaxing the assumption of fixed position in the fit and by fitting using an elliptical Gaussian, we are able to minimize their effects using OLS. The computational speed of OLS is quite acceptable (58 molecular fits per second for a 2.40GHz processor). Finally, the performance of OLS for low photon counts was observed to be better than aperture photometry. However, for low surface density of molecules and high signal-to-noise, aperture photometry is a fast alternative method.

The ideal solution to photon-counting for tFRET is a profile fitting approach which has the advantages described for OLS, but which also obtains optimal signal-to-noise. A recent report by Mortensen by al. (39) shows that maximum-likelihood methods (43) may be just that approach; it should be straightforward to adapt our software to use these methods.

Filtering

A significant concern for the analysis of surface-immobilized molecules is to exclude errors introduced by overlapping unresolved molecules. We show that filtering based on nearest-neighbor distance and shape is sufficient to obtain performance at a level better than the Rayleigh criterion.

We use two metrics to identify and exclude overlapping molecules. The first is the nearest-neighbor distance between resolved molecules in any channel, based on the position of molecules in the image used for autodetection. Any resolved molecules with too small separation will significantly affect the measured photon-counts for each molecule, so they are excluded. Secondly, we calculate the eccentricity of each molecular PSF, for each individual frame (34),

$$\epsilon = \sqrt{1 - \frac{s_y^2}{s_x^2}}, \tag{S23}$$

where s_y and s_x are the PSF widths along the major and minor axes respectively, defined in Eq. 7. Monitoring the eccentricity on a per-frame basis has the additional advantage of providing a robust means to test whether sections of a recorded dataset are significantly out of focus (these sections can then be excluded from analysis if necessary).

We tested our ability to efficiently filter overlapping molecules in Monte Carlo simulated datasets. We simulated molecules with uniform photon count M=5000 photons/molecule per frame, and fixed surface density, n molecules μm^{-2}, with a uniform random spatial distribution. Images were generated for a 256x256 pixel imaging grid with pixel size of 94 nm and PSF width of 132 nm, to match typical experimental values for the donor-emission channel. Other simulation parameters were as previously described. Image analysis was carried out as described above, including calculation of a 10-frame-averaged image for auto-detection and calculation of nearest-neighbor distance.

We first tested the effectiveness of eccentricity filtering for a random distribution of particles at moderate density (0.86 molecules μm^{-2}). We segregated the detected points into correctly identified single molecules, and multiple molecules incorrectly identified as a single molecule using distance-based hierarchical clustering (31). We calculated the resulting eccentricity distributions for each case (Figure S4A). The distribution including both unresolved and resolved molecules

separates into two clear peaks, and the vast majority of overlapping molecules may be excluded by a simple threshold on eccentricity after visual inspection of the eccentricity distribution.

We tested the efficiency of filtering (including both nearest-neighbor distance and eccentricity) in improving photon-counting accuracy, and compared it with the performance we would expect from a Rayleigh-criterion limited technique. The Rayleigh-limit for a visible light microscope is approximately $\lambda/2$ (44, 45). For Gaussian PSFs, this roughly corresponds to $\Delta x_{min} \sim 2s$ (s is the PSF width), which we use here as our reference standard for a filtering algorithm with Rayleigh-limit performance. We assume that the photon count observed for multiple unresolved molecules is simply the sum of their individual photon counts. For a surface density of n molecules per unit area, we derived an expression for the root-mean-square (RMS) photon-counting error of a theoretical Rayleigh-limit performance filtering algorithm based on simple Poisson statistics:

$$\frac{\Delta M_{rms}}{M_{true}} = \sqrt{\frac{1 - e^{-\mu} - \mu + \mu^2}{1 - e^{-\mu}}}, \quad \mu = 4\pi s^2 n. \tag{S24}$$

We analyzed the observed photon-counting errors for a wide range of surface densities (Figure S4B), and the effect of different filtering thresholds. Without filtering, photon-counting errors are approximately at the same level as Rayleigh-limit performance. If we apply a standard eccentricity threshold of $\epsilon \leq 0.6$ (see Figure S4A), and different nearest-neighbor thresholds, we observe significantly smaller photon-counting errors than the Rayleigh-limit level. Since higher thresholds lead to the exclusion of a larger fraction of candidate molecules, in many cases a low nearest-neighbor threshold of $4s$ is entirely sufficient to give good performance at moderate surface density. For maximum accuracy, a higher threshold of $6s$ reduces photon-counting errors even further.

Supporting figures
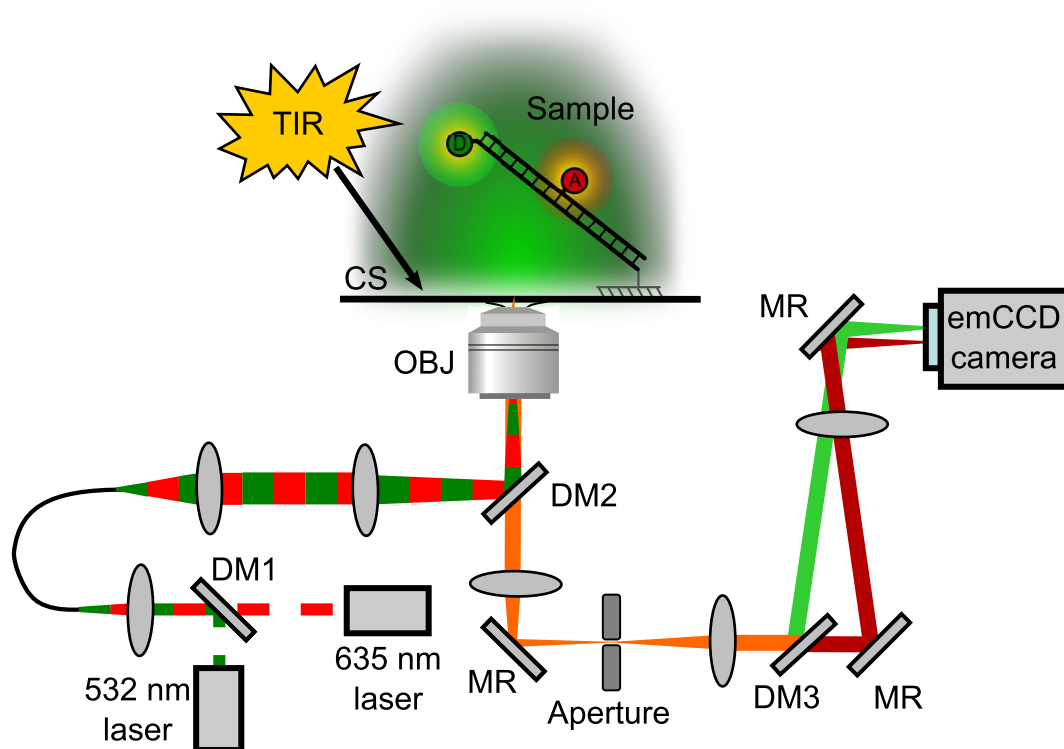
Figure S1: *Apparatus for tFRET.* Modulated 532 nm and 635 nm lasers are combined into an optical fiber and excite a surface-immobilized sample in TIRF mode. Fluorescence emission is collected and imaged onto an emCCD camera. DM, dichroic mirror; BS, beam-splitter; OBJ, objective lens; CS, coverslip; TIR, Total Internal Reflection; MR, mirror; emCCD, electron-multiplying charge-coupled device.
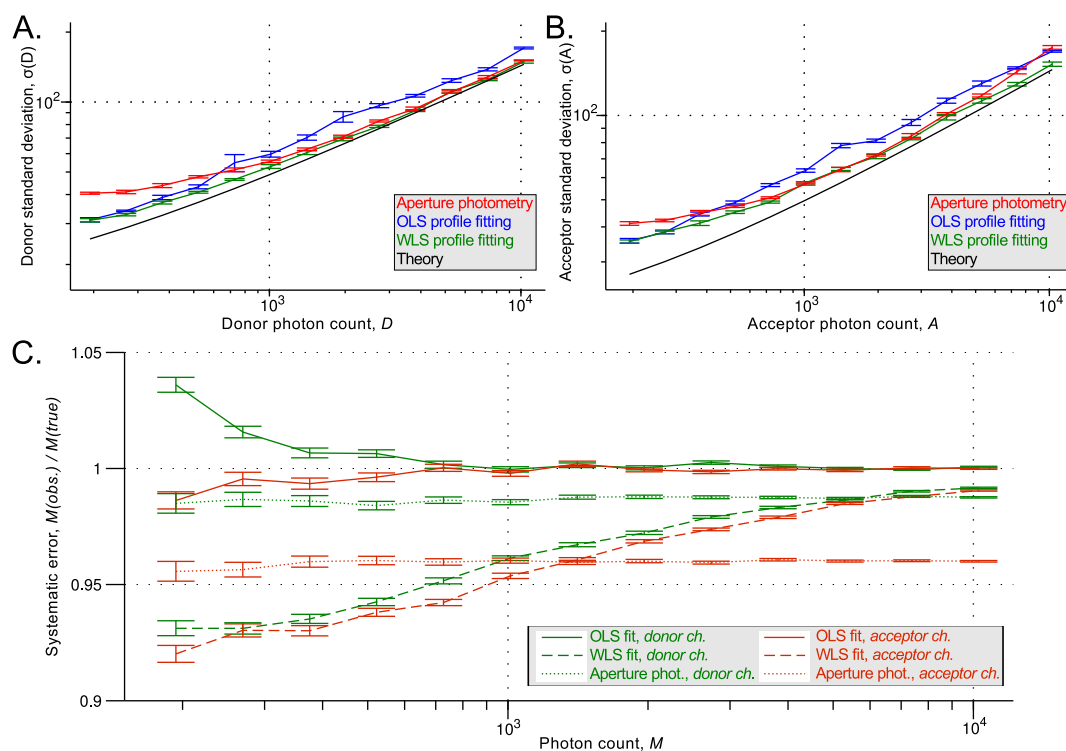
Figure S2: *Photon counting performance of different photometry methods. A-B.* Photon counting standard deviation for increasing photon count. *A.* Simulations for typical PSF width of donor channel, 132 nm. *B.* Simulations for typical PSF width of acceptor channel, 150 nm. *C.* Systematic photon-counting error for increasing photon count. *Green lines*, simulations for donor channel, PSF width 132 nm; *red lines*, simulations for acceptor channel, PSF width 150 nm. *Solid lines*, OLS minimization results; *dashed lines*, WLS minimization results; *dotted lines*, aperture photometry results.
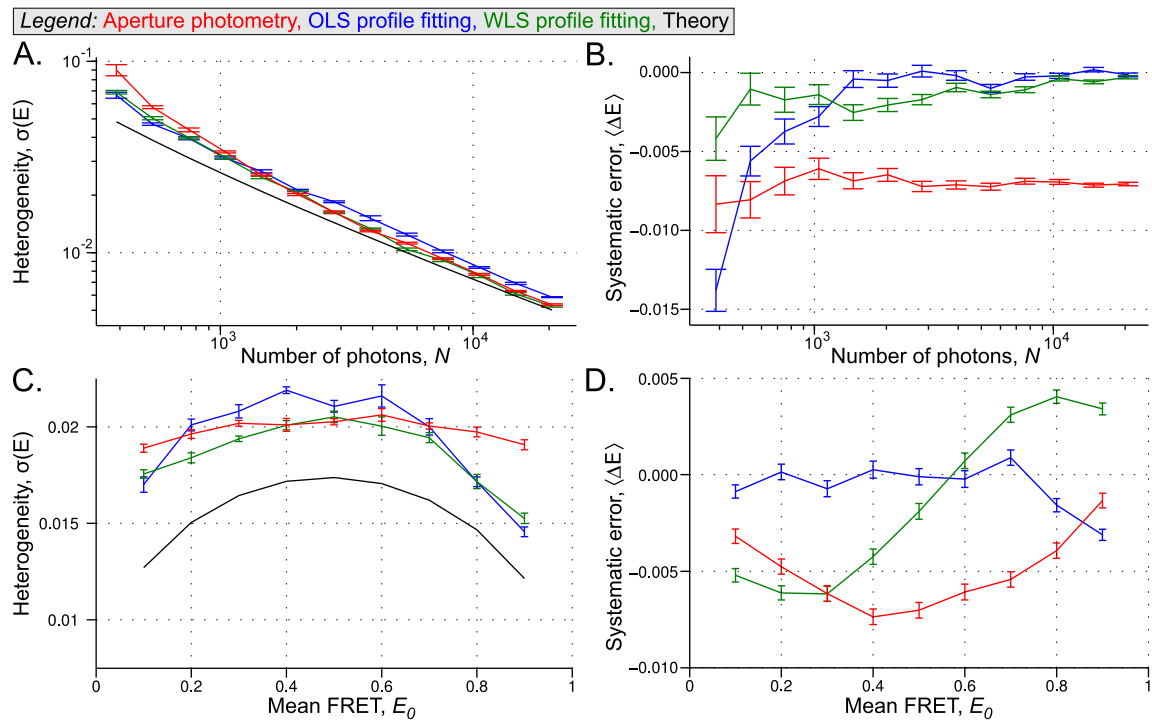
Figure S3: *FRET error for different photometry methods. Red line*, aperture photometry; *blue line*, OLS minimization; *green line*, WLS minimization; *black line*, theoretical predictions. PSF width in donor channel, s=132 nm, PSF width in acceptor channel, s=150 nm. *A-B*. FRET standard deviation and systematic error for increasing photon count, mean FRET 0.5. *C-D*. FRET standard deviation and systematic error for varying E_0, total photon count per molecule, 2000 photons.
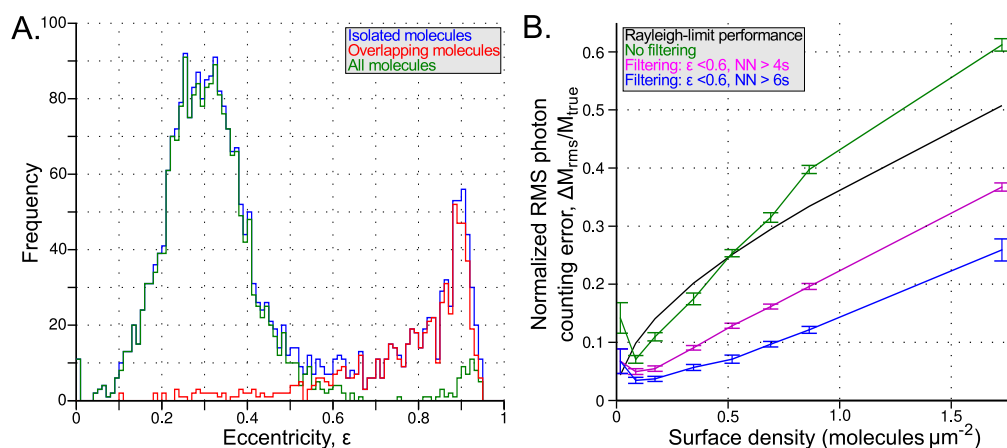
Figure S4: *Thresholding based on eccentricity and nearest-neighbor distributions allows discrimination of overlapping molecules with super-Rayleigh-limit performance. A*. Analysis of the eccentricity distribution for a simulated dataset with moderate surface density (0.86 molecules μm^{-2}). Distribution for all detected positions (*green line*) is compared with the known stoichiometry of the simulated molecules: isolated particle (*blue line*), multiple overlapping molecules (*red line*). By filtering all molecules after the first major peak in the eccentricity distribution ($\epsilon < 0.6$), we are able to exclude most overlapping molecules. *B*. Effect of filtering on normalized RMS photon-counting error for simulated datasets of increasing surface density. *Black line*, photon-counting error assuming Rayleigh-limit performance; *green line*, unfiltered molecules; *pink line*, filtered molecules, minimum nearest-neighbor distance $> 4s$; *blue line*, filtered molecules, minimum nearest-neighbor distance $> 6s$ (s is width of molecular PSF). $\epsilon < 0.6$ for both filtered datasets.
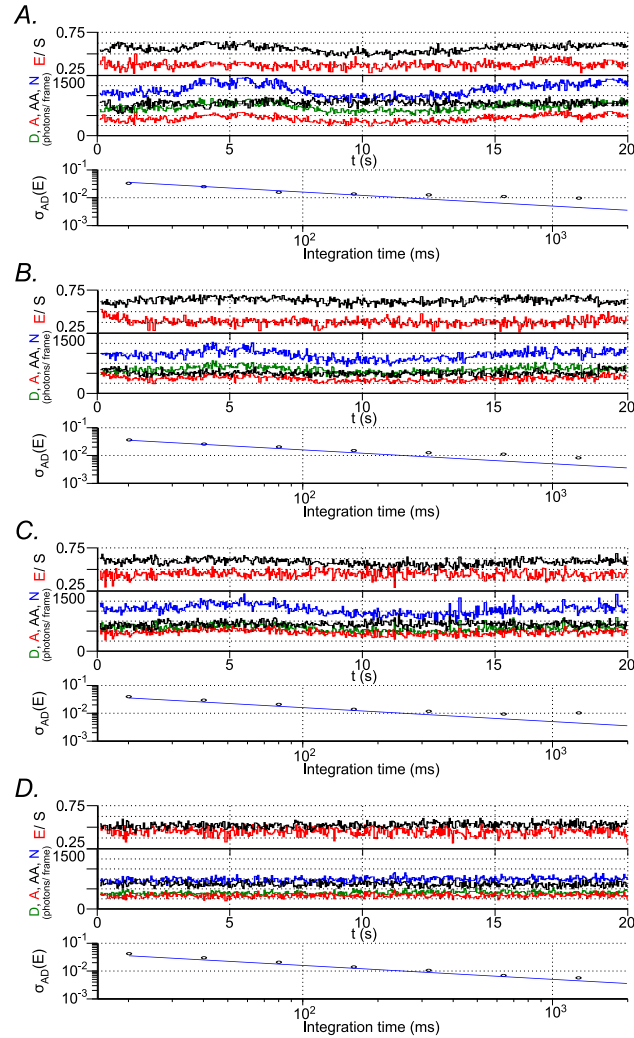
Figure S5: *Focal drift within a single FOV causes excess dynamic heterogeneity. A-C.* Examples of molecules from a single FOV showing slow correlated fluctuations in total photon count N, and excess dynamic heterogeneity, consistent with the source being focal drift. Interestingly, not all molecules within a single FOV appear to be affected by focal drift; an exemplar molecule shown in *D*, from the same FOV as the molecules shown in *A-C* shows stable photon counts and FRET over the whole measurement. For the FOV shown here, only ~13 out of 42 molecules within the FOV appeared to be affected by focal drift.

Supporting Tables

Sample	Cy3B anisotropy	ATTO647N anisotropy
Cy3B	0.04	N/A
T1B16	0.20	0.15
T1B18	0.22	0.16
T1B18GC	0.22	0.15
T1B18INT	0.22	0.17

Table S1: *Ensemble fluorescence anisotropy measurements for dsDNA standards show similar anisotropy for all samples.* The control sample, free Cy3B-NHS ester, showed very low anisotropy consistent with high rotational freedom. All dsDNA FRET standards show increased anisotropy (consistent with slow global rotation of dsDNA), but anisotropy is not sufficiently large to suggest restricted rotational freedom of the fluorophores on the millisecond timescale. Anisotropy is similar for all dsDNA standards suggesting no change in rotational freedom of the dyes between the samples. Measurements carried out in PBS buffer. Cy3B anisotropy measurements were carried out at 540 nm excitation, 580 nm emission. ATTO647N measurements were carried out at 635 nm excitation, 675 nm emission.

References

1. Thompson, R. E., D. R. Larson, and W. W. Webb, 2002. Precise nanometer localization analysis for individual fluorescent probes. *Biophys. J.* 82:2775–2783.

2. Taylor, J., 1997. An introduction to error analysis: the study of uncertainties in physical measurements. University Science Books, Herndon, VA.

3. Howell, S. B., 2006. Handbook of CCD Astronomy. Cambridge University Press, Cambridge, UK.

4. Robbins, M., and B. Hadwen, 2003. The noise performance of electron multiplying charge-coupled devices. *IEEE T. Electron. Dev.* 50:1227 – 1232.

5. E2V Technologies. Low Light Technical Note 5: An Overview of the Ageing Characteristics of L3Vision Sensors. `http://www.e2v.com`, Accessed on 24 Jun. 2010.

6. Tulloch, S. M., 2004. Photon counting and fast photometry with L3 CCDs. *In* Ground-based Instrumentation for Astronomy. SPIE, Bellingham, WA.

7. Ulbrich, M. H., and E. Y. Isacoff, 2007. Subunit counting in membrane-bound proteins. *Nat. Methods* 4:319–321.

8. Hogg, R., and A. Craig, 1978. Introduction to mathematical statistics. McMillan, New York, NY.

9. Deniz, A. A., T. A. Laurence, M. Dahan, D. S. Chemla, P. G. Schultz, and S. Weiss, 2001. Ratiometric single-molecule studies of freely diffusing biomolecules. *Annu. Rev. Phys. Chem.* 52:233–53.

10. Kapanidis, A. N., N. K. Lee, T. A. Laurence, S. Doose, E. Margeat, and S. Weiss, 2004. Fluorescence-aided molecule sorting: Analysis of structure and interactions by alternating-laser excitation of single molecules. *Proc. Natl. Acad. Sci. U.S.A.* 101:8936–8941.

11. Santoso, Y., L. C. Hwang, L. Le Reste, and A. N. Kapanidis, 2008. Red light, green light: probing single molecules using alternating-laser excitation. *Biochem. Soc. Trans.* 036:738–744.

12. Holden, S. J., and A. N. Kapanidis, 2009. Alternating-Laser Excitation and Pulsed-Interleaved Excitation of Single Molecules. *In* Single Particle Tracking and Single Molecule Energy Transfer: Applications in the Bio and Nano Sciences. Wiley-VHC, Berlin, Germany.

13. Axelrod, D., 2001. Total internal reflection fluorescence microscopy in cell biology. *Traffic* 2:764–774.

14. Zhuang, X., L. E. Bartley, H. P. Babcock, R. Russell, T. Ha, D. Herschlag, and S. Chu, 2000. A Single-Molecule Study of RNA Catalysis and Folding. *Science* 288:2048–2051.

15. Joo, C., and T. Ha, 2008. Single-Molecule FRET with Total Internal Reflection Microscopy. *In* Single-molecule techniques: a laboratory manual. CSHL Press, Cold Spring Harbor, NY.

16. Gopich, I. V., and A. Szabo, 2007. Single-Molecule FRET with Diffusion and Conformational Dynamics. *J. Phys. Chem. B* 111:12925–12932.

17. Tubbs, R. N., 2004. Lucky exposures: diffraction-limited astronomical imaging through the atmosphere. Ph.D. thesis, University of Cambridge (UK).

18. Neumann, J. V., 1951. Various techniques used in connection with random digits. *Applied Math Series* 12:36–38.

19. Roy, R., S. Hohng, and T. Ha, 2008. A practical guide to single-molecule FRET. *Nat. Methods* 5:507–516.

20. Schluesche, P., G. Stelzer, E. Piaia, D. C. Lamb, and M. Meisterernst, 2007. NC2 mobilizes TBP on core promoter TATA boxes. *Nat. Struct. Mol. Biol.* 14:1196–1201.

21. Solomatin, S. V., M. Greenfeld, S. Chu, and D. Herschlag, 2010. Multiple native states reveal persistent ruggedness of an RNA folding landscape. *Nature* 463:681–684.

22. Crocker, J. C., and D. G. Grier, 1996. Methods of Digital Video Microscopy for Colloidal Studies. *J. Colloid Interface Sci.* 179:298–310.

23. Irwin, M. J., 1985. Automatic analysis of crowded fields. *Mon. Not. R. Astron. Soc.* 214.

24. Irwin, M. J., 1997. Detectors and Data Analysis Techniques for Wide Field Optical Imaging. *Instrumentation for large telescopes: VII Canary Islands Winter School of Astrophysics* 35.

25. Buonanno, R., and G. Iannicola, 1989. Stellar photometry with big pixels. *Pub. A. S. P.* 101:294–301.

26. Stetson, P. B., 1987. DAOPHOT: A computer program for crowded-field stellar photometry. *Pub. A. S. P.* 99:191–222.

27. Merline, W. J., and S. B. Howell, 1995. A realistic model for point-sources imaged on array detectors: The model and initial results. *Exp. Astron.* 6:163–210.

28. Churchman, L. S., Z. Ökten, R. S. Rock, J. F. Dawson, and J. A. Spudich, 2005. Single molecule high-resolution colocalization of Cy3 and Cy5 attached to macromolecules measures intramolecular distances through time. *Proc. Natl. Acad. Sci. U.S.A.* 102:1419–1423.

29. Groth, E. J., 1986. A pattern-matching algorithm for two-dimensional coordinate lists. *Astron. J.* 91.

30. Murtagh, F., 1992. A new approach to point-pattern matching. *Pub. A. S. P.* 104:301–307.

31. Hastie, T., R. Tibshirani, and J. Friedman, 2001. The elements of statistical learning: data mining, inference, and prediction. Springer-Verlag, New York, NY.

32. Yildiz, A., J. N. Forkey, S. A. McKinney, T. Ha, Y. E. Goldman, and P. R. Selvin, 2003. Myosin V walks hand-over-hand: single fluorophore imaging with 1.5-nm localization. *Science* 300:2061–2065.

33. Cheezum, M. K., W. Walker, and W. H. Guilford, 2001. Quantitative comparison of algorithms for tracking single fluorescent particles. *Biophys. J.* 81:2378–2388.

34. Rust, M. J., M. Bates, and X. Zhuang, 2006. Sub-diffraction-limit imaging by stochastic optical reconstruction microscopy (STORM). *Nat. Methods* 3:793.

35. Janes, K. A., and J. N. Heasley, 1993. Stellar Photometry Software. *Pub. A. S. P.* 105:527–537.

36. Lourakis, M. I. A. levmar: Levenberg-Marquardt nonlinear least squares algorithms in C/C++. `http://www.ics.forth.gr/~lourakis/levmar/`, Accessed on 1 Oct. 2009.

37. Dennis, J., and R. Schnabel, 1996. Numerical methods for unconstrained optimization and nonlinear equations. Society for Industrial and Applied Mathematics, Philadelphia, PA.

38. Howell, S. B., 1989. Two-dimensional aperture photometry - Signal-to-noise ratio of point-source observations and optimal data-extraction techniques. *Pub. A. S. P.* 101:616–622.

39. Mortensen, K. I., L. S. Churchman, J. A. Spudich, and H. Flyvbjerg, 2010. Optimized localization analysis for single-molecule tracking and super-resolution microscopy. *Nat. Methods* 7:377–381.

40. Price, P. F., 1979. A comparison of the least-squares and maximum-likelihood estimators for counts of radiation quanta which follow a Poisson distribution. *Acta Crystallogr. A* 35:57–60.

41. Baker, S., and R. D. Cousins, 1984. Clarification of the use of chi-square and likelihood functions in fits to histograms. *Nucl. Instrum. Methods* 221:437 – 442.

42. Stetson, P. B., 1990. On the growth-curve method for calibrating stellar photometry with CCDs. *Pub. A. S. P.* 102:932–948.

43. Ferguson, T. S., 1996. A course in large sample theory. CRC Press, Boca Raton, FL.

44. James, J., 1976. Light microscopic techniques in biology and medicine. Springer, New York, NY.

45. Hecht, E., 1998. Optics. Addison-Wesley, Reading, MA.